Catena 233 (2023) 107531

Contents lists available at ScienceDirect

Catena

journal homepage: www.elsevier.com/locate/catena

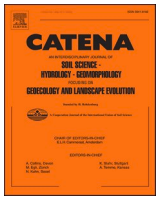

The Quaternary activity of the Estella diapir from the uplift record of fluvial terraces, pediments and cave sediments in the Western Pyrenees, Spain

Jesús Guerrero [a,*], Miguel Bartolomé [b], Ergin Gökkaya [c]

[a] University of Zaragoza. Department of Earth Sciences, Spain
[b] National Science Museum of Madrid, Spain
[c] University of Ankara, Department of Geography, Turkiye

ARTICLE INFO

Keywords:
Salt tectonics
Deformation rates
Gypsum cave
Erosional unloading
Collapse sinkhole
River salinity

ABSTRACT

This work analyses the Quaternary landforms, geomorphic changes and stratigraphic evidences of evaporite dissolution and halokinesis in the Estella salt diapir (Basque-Cantabrian Basin). The mapping of Quaternary deposits demonstrates that karstic subsidence and diapirism happen at the same time. The diapir geometry is characterised by a prominent 4.5 km-long fault scarp attributed to the uplift of the diapir and a fluvial gypsum escarpment along the northern and eastern diapir edges. The dissolution of the gypsiferous caprock is responsible for the development of a large number of collapse sinkholes, the local thickening of terrace deposits and a network of endokarstic conduits connected to saline springs that cause a notable increase in the salinity of the Ega river across the diapir (70% electrical conductivity increase). The 40 m vertical displacement of T4 terrace and P5 pediment deposits, the anomalous longitudinal profile of the old terraces, the deflection of infilled-valleys at the base of the fault scarp, the occurrence of wind gaps and the continuous lateral migration of the Ega river away from the diapir support salt upwelling since 644 ± 81 ka ago at a long-term, average uplift rate of 0.05–0.07 mm/yr. The 12 m offset of T8 terrace, the steepening of the Ega river floodplain and the tilting of the upper level and the antigravitative erosion genesis of the Longinos cave point to a faster diapir rising rate of 0.23–0.57 mm/yr in the last 36 ± 15 ka coinciding with a period of increasing river incision. The lack of tectonic activity in the region suggests that diapirism is enhanced by erosional unloading related to fluvial entrenchment. The thickening of pediment P5 supports the north-northeast flow of salt towards the river valley.

1. Introduction

Salt diapirs, salt stocks or salt plugs are defined as circular to elliptical-shaped, bodies of salt that have flowed in a ductile manner and show discordant contacts with the overlying strata (Hudec and Jackson, 2007). These salt structures have been described in all continents such as in the Atlas range and Gabon and Congo sedimentary coastal basins in Africa (eg: Rouby et al., 2002; Boubaya et al., 2011), in Texas and Paradox basins and Gulf of Mexico in North America (eg: Trudgill, 2011; Rowan et al, 2012), in the Permian Basin and Hellenitic arc in Europe (eg: van Hinsbergen et al., 2006; Warsitzka et al., 2015), in the Death Sea, Zagros Mountains and China in Asia (eg: Talbot and Aftabi, 2004; Bruthans et al., 2010; Adeoti and Webb, 2022), offshore Brazil in South America (Luca et al., 2017) and in Australia in Oceania (eg: Backé et al., 2010). In addition, they have an important economic interest in the oil and gas industry for the exploitation of hydrocarbons (Hudec and Jackson, 2011 and references therein) and in the mining industry providing salt, potash or even ore deposits (Warren, 2016 and references therein). There is also an extensive literature dealing with salt structures in regional tectonics and sedimentary basin evolution in non-petroleum provinces (eg: Dooley et al., 2009; Santolaria et al., 2015; Camara, 2020). In contrast, their Quaternary activity have not received the same geological investigation despite their relevant practical implications for waste disposal (Baikpour et al., 2016), seismic and landslide hazards (Dahm et al, 2011; Gutiérrez and Lizaga, 2016) and water salinization (Jalali et al., 2019; Abedi et al., 2021). The current rising of salt diapirs due to salt upwelling is responsible for the doming and faulting of the diapir roof and the subsidence of salt withdrawals basins (Stewart, 2006). These earth-surface processes cause notable changes in the landscape including the development of subsidence depressions, fissures and faults due to the deformation of the overburden (Stewart, 2006; Dooley et al., 2009), changes in the drainage network (Guerrero et al.,

* Corresponding author.
E-mail addresses: jgiturbe@unizar.es (J. Guerrero), mbartucar@gmail.com (M. Bartolomé), erginngokkaya@gmail.com (E. Gökkaya).

https://doi.org/10.1016/j.catena.2023.107531
Received 24 May 2023; Received in revised form 11 September 2023; Accepted 14 September 2023
Available online 23 September 2023

2015, 2017; Gutiérrez et al., 2019); slopes steepening and landslide formation (Gutiérrez and Lizaga, 2016) and the uplift, arching and tilting of Quaternary markers such as fluvial terraces (Lucha et al., 2012; Jochems and Pederson, 2015; Gutiérrez et al., 2019), marine terraces (Bruthans et al., 2006) and caves (Frumkin, 1996; Bruthans et al., 2010).

In Spain, salt diapirs are present in most of the mountain ranges including the Pyrenees and the Betics (De Ruig, 1995; Serrano and Martínez del Olmo, 2004; Lucha et al., 2008; Santolaria et al., 2015). In the Pyrenees, the Basque-Cantabrian basin hosts a large number of Triassic, tectonic-related salt stocks (Barnolas and Pujalte, 2004; Ferrer et al., 2012; Poprawski et al., 2014). These salt-structures have been subject to an intensive drilling and geophysical survey for oil exploration (Serrano and Martinez del Olmo, 2004; Marín-Barba et al., 2014) that have helped to understand the stratigraphy and structure of the basin (Salvany, 1990; Muñoz, 1992; García-Mondejar, 1996) and the rifting and inversion processes of the orogen (Jammes et al., 2010; Ferrer et al., 2012; Lescoutre et al., 2020; Lescoutre et al., 2021; Miró et al., 2020, Miró et al.,2021). In addition, a large number of works focused on the evolution and structural arrangement of these salt structures integrating surface geology and subsurface data (Larrasoaña, 2003; Pinto et al., 2005; Poprawski et al., 2014, 2016; Guerrero et al., 2017, Guerrero et al., 2019; Camara, 2020). However, none of the research studies deals with the current activity of salt diapirs recorded by the deformation of Quaternary landforms and deposits and the control exerted by salt flow on the present landscape.

This is the first work analysing the present activity of salt-structures in the Basque-Cantabrian basin using geomorphological markers and integrating geological mapping, hydrochemical data and cave speleogenesis. The study area focuses on the upper-middle 25 km-long reach of the Ega river, a 60 km-long Pyrenean tributary of the Ebro river that dissects the Estella diapir. Here, subsidence and diapirism are responsible for drainage disruption, the arching and thickening of the fluvial sediments, the offset of pediment deposits and the steeping and abandonment of cave passages. The main objectives of the investigation include: 1) calculate the growing rates of Estella diapir since the Middle Pleistocene, 2) understand the geomorphological implications of salt upwelling in the landscape, 3) assess the effects of diapir karstification on the Ega river salinity and 4) describe the origin and evolution of the Longinos gypsum cave. Despite gypsum dissolves much faster than limestone (Dreybrodt, 2004; Ford and Williams, 2007), its low mechanical strength favours the rapid destruction and obstruction of gypsum passages by breakdown processes (Palmer, 2009) and consequently the number of gypsum caves reported in Spain is very low. Some examples are the Agua and Covadura caves in the Sorbas Basin (Calaforra and Pulido-Bosch, 1996), the Pedro Fernández Cave in the Tajo Basin (Almendros and Antón, 1983), and the Borro and Mosquera Caves in the Fluvia valley (Gutiérrez et al., 2016). So far, the Longinos cave is the only known gypsum cave in the Basque-Cantabrian basin.

The area shows a Mediterranean subhumid climate with an average annual rainfall rate of around 750 mm where the soil is under saturated conditions half of the year (Urabayen and Chasco, 2001). The sedimentary record of peat bogs and lakes and the establishment of mixed deciduous forests in the studied area point to similar humid conditions since the last 11.9 ka with century-to-millennial wetter intervals than today (Corella et al., 2013; Sánchez-Morales et al., 2022 and references within).

2. Study site

The Basque-Cantabrian basin is located in the Western Pyrenees to the west of the Pamplona Fault. This NE-SW trending, 120 km-long, non-outcropping basement fault marks the boundary between the Basque-Cantabrian Basin in the Western Pyrenees and the Jaca-Pamplona Basin in the Central Pyrenees (Fig. 1). The Basque-Cantabrian Basin shows a complex geology related to the overlapping of extensional and compressional phases. This complexity made Barnolas and Pujalte (2004) divide the basin into three geological provinces separated by thrust faults named from west to east: Norcastellana Platform, Navarro-Cantabro trough and Vasco Arc (Fig. 1). The South Pyrenean Thrust and the Oco and Learza faults constitute the boundary of the Navarro-Cantabro Trough with the Ebro Foreland Basin (Fig. 1). The Basque-Cantabrian basin contains more than 50 Triassic, tectonic-related, salt-cored anticlines, salt walls and salt stocks that were triggered under extensional regime during the Upper Jurassic-Lower Cretaceous rifting in relation to the opening of the North Atlantic and Bay of Biscay (García-Mondéjar, 1996; Vergés et al., 2002). Subsequently, during the Alpine compression in the Late Cretaceous and Cenozoic, they were squeezed and finally pierced the overburden with NE-SW and E-W orientations coinciding with the shortening direction and the trace of the major basement faults and thrust sheets (Salvany, 1990; Muñoz, 1992; Serrano and Martinez del Olmo, 2004; Ferrer et al., 2012; Poprawski et al., 2014).

At the end of the Miocene, the Ebro foreland basin was captured by a primitive Ebro river that started to dissect the endorheic basin fill (García-Castellanos et al., 2003; Pérez-Rivarés et al., 2004). The upstream propagation of its incision wave from the Mediterranean Sea to

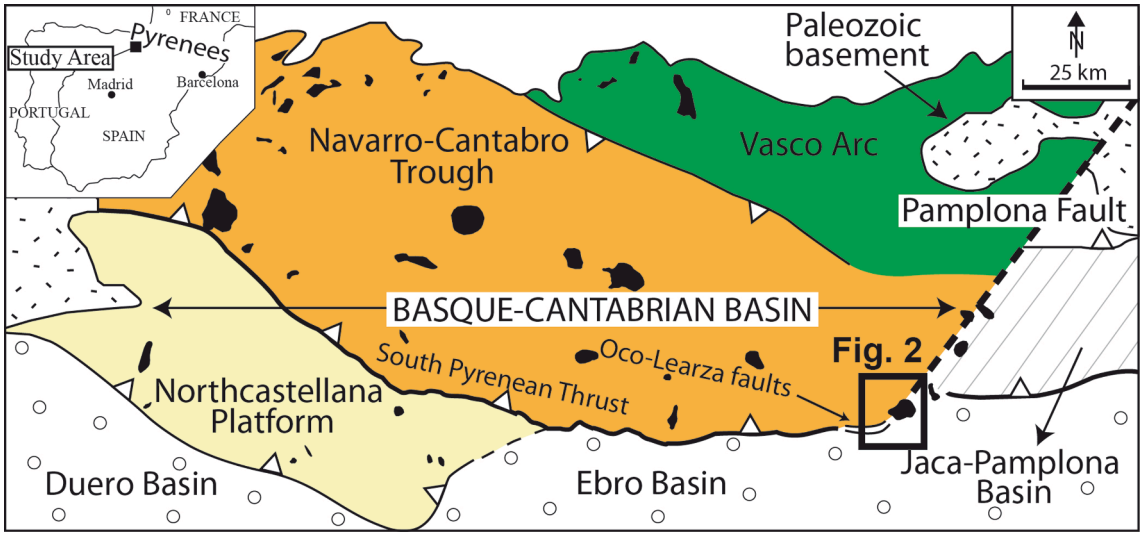

Fig. 1. Geological sketch of the Basque-Cantabrian basin showing its three main domains (Norcastellana Platform, Navarro-Cantabro trough and Vasco Arc) (modified from Barnolas and Pujalte, 2004). Black polygons indicate the location of the main salt structures.

its headwaters combined with climatic oscillations led to the development of a new network of tributaries, fluvial valleys and staircase terrace and pediment sequences. The existence of high alluvial terraces over 160 m above the present Ebro river thalweg close to its headwaters with a minimum Electron Spin Resonance age over 1.2 Ma points to a well-established drainage network at the Early Pleistocene (Parés et al., 2021; Benito-Calvo et al., 2022). Since then, the outcropping salt started to dissolve and salt diapirs and anticlines subsided to become crater-shaped landforms up to 300 m deep below their annular rings. As a testimony of this ongoing karstification process, most of salt structures host a well-developed endokarst hydraulically connected to high-salinity springs whose waters are diverted towards evaporation ponds for the exploitation of salt (Iribar and Abalos, 2011; Guerrero et al., 2017, 2019; Abalos et al., 2008). This karstification phenomenon often overlaps with salt migration and upwelling in the region that seems to be enhanced by erosional unloading related to fluvial entrenchment (Guerrero et al., 2017). The prevalence of either salt-dissolution subsidence or diapirism defines their final geometry and the present structural configuration of the diapirs roof.

The Estella diapir is a NE-SW-oriented, elongated, vertical-wall, salt stock that is located at the eastern margin of the Navarro-Cantabro trough, truncating the Oco-Learza normal faults at the southern margin and aligned along the Pamplona Fault (Figs. 1 and 2). Its structure and stratigraphy has been studied in detail by Pflug (1973), Pflug and Schöll (1976), IGME (1978aand b) and Olive et al. (2010a,b). Its uplift started during the Albiense and continued during the Alpine compression at the upper Cretaceous, Middle Eocene and mainly at the end of the Oligocene-beginning of the Miocene when it finally pierced a thick sedimentary sequence constituted by more than 3 km of Cretaceous limestones and marls, 200 m of Paleocene-Eocene platform limestones and several kilometres thick Oligocene-Miocene synorogenic alluvial fan facies that unconformably lies on the Mesozoic and Tertiary carbonate layers (Pflug, 1973; Uranga et al., 1997; Olive et al., 2010a, b). This stratigraphic sequence is steeply dipping around the diapir flanks leading to subvertical vertical ridges that progressively decrease their dip away from the diapir to less than 5-20° to grade into gentle dip slopes, especially on its southern flank (Fig. 2, cross-section). Deep boreholes and seismic reflection profiles for hydrocarbon exploration evidence that the thickness of the Triassic evaporites at the Estella diapir reaches more than 3500 m due to salt migration (Fig. 2), extending to the west along the Ega river valley and abruptly decreasing to the south and east (Serrano and Martinez del Olmo, 2004; IGME, 1990a,b). At the

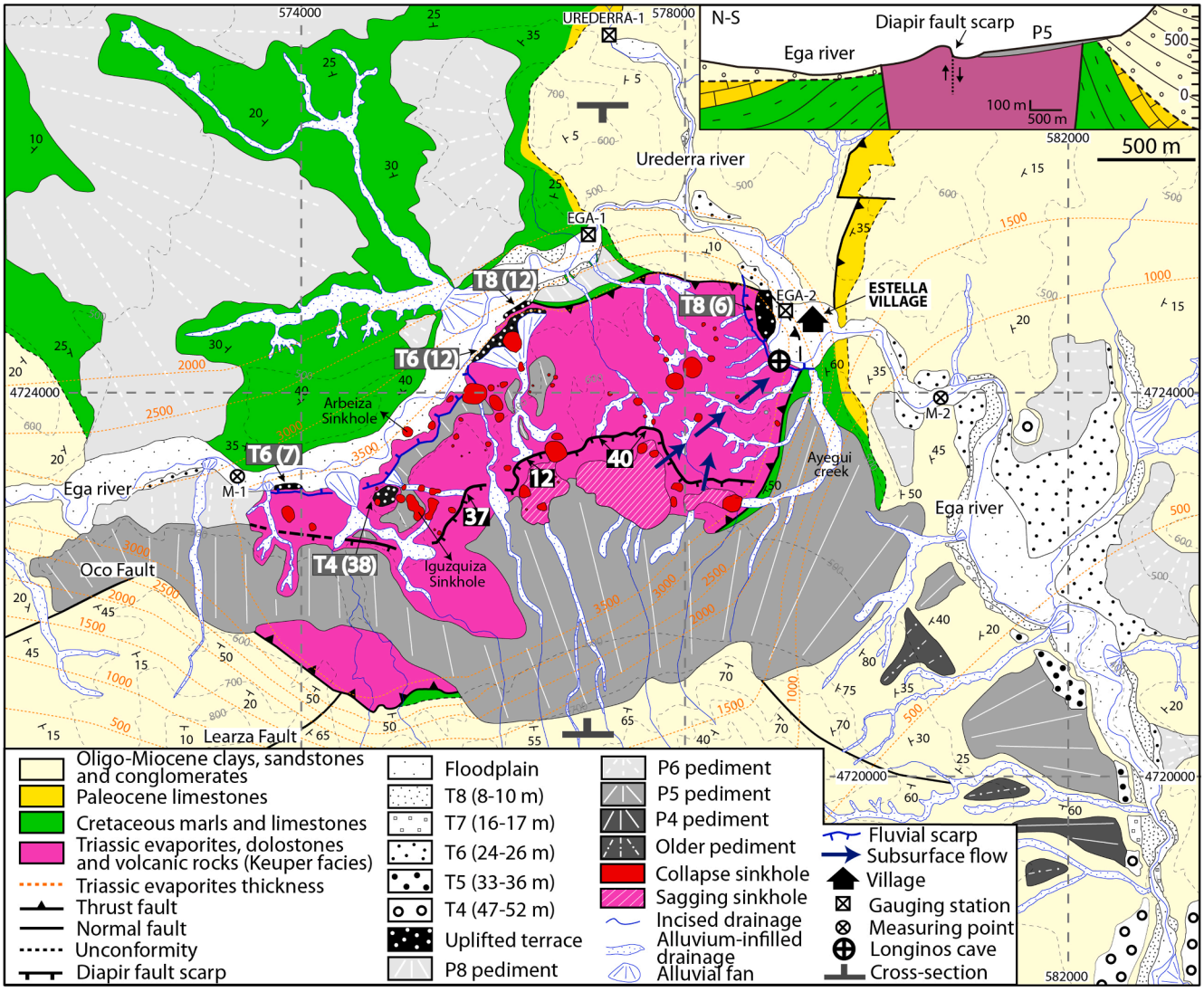

Fig. 2. Geomorphological map of the Estella diapir with the location of the gauging stations and measuring points, the uplifted terraces, the offset of the infilled-valleys and the diapir fault scarp. The dark-grey crosses mark the trace of the cross-section displayed on the upper-right corner. Numbers inside black squares along the fault scarp represent the vertical uplift of infilled-valleys. Letters and numbers in brackets inside dark grey squares show the level and vertical thrown of uplifted terraces, respectively. (UTM European Terrestrial Reference System 1989; ETRS 1989).

surface, salt beds have been already dissolved leading to a thick Triassic dissolution residue made up of a distorted mass of anhydrite, gypsum, shale, dolomite and intruded mafic volcanic rocks that cover the diapir crest (Olive et al., 2010a,b).

3. Material and methods

The applied methods include: i) the geomorphological mapping of the Quaternary deposits and karstic landforms, cave topography and sediments descriptions, ii) the measurement of sinkhole morphometric parameters, iii) the analysis of time-series hydrological and hydrochemical data of the Longinos saline spring, the Ega river and its main tributary (Urederra river), and iv) the radiocarbon dating of two detrital sequences hosted in the Longinos cave.

The geomorphological map is based on the interpretation of colour stereoscopic aerial photographs of 2018 with a 25 cm pixel resolution printed at a scale of 1:10,000 and a 1 m pixel resolution digital elevation model (DEM) derived from the 2016 LiDAR data with a density of 14 measuring points per square meter and with a mean square error in the horizontal and vertical axes of 20 and 15 cm, respectively downloaded from the Spanish National Geographic Institute (IGN). The LiDAR-derived DEM was produced from the bare-ground data using the ArcGIS tool "Las Dataset to Raster" and the triangulation method. The preliminary geomorphological map was checked and refined in the field using colour 1:5,000 scale orthophotographs. The geological database was developed on a Geographical Information System (ArcGIS 10.7) using 25 cm pixel size orthoimages from the IGN. The bedrock geology, the thickness of Triassic evaporites and the geological cross-sections were based on borehole and seismic reflection profiles provided by the Spanish Geological Survey (IGME, 1990a,b) and IGME (1978a and b) and Olive et al. (2010a,b) geological maps. The mapping of the Ega terraces was based on their lateral continuity along the valley rather than on their relative height above the river channel. The height of the terrace remnants was calculated from the 2016 LiDAR data.

The LiDAR-derived DEM was used to extract the main morphometric parameters of the sinkholes (major axis, orientation of the major axis, area, elongation ratio, perimeter, circularity ratio, mean elevation of the perimeter, volume, elevation of deepest point and depth) following the procedure described by Parenti et al. (2020). Table 1 includes the maximum, minimum, average values and standard deviation of some of the parameters. The azimuth of the major axis of the depressions was plotted on a rose diagram using the GeoRose software. The frequency-size relationship of the depressions has been analysed considering their major axis generating the best-fit regression function following the methodology described by (Taheri et al., 2015). The Nearest Average Neighbour tool was used to analyse their spatial distribution.

Time-series electrical conductivity and salinity values of the Longinos saline spring together with the average conductivity, hydrochemical values and daily average discharge of the Ega and Urederra rivers at their gauging stations (Ega-1, Ega-2 and Urederra-1; see locations at Fig. 2) and measuring points (M−1 and M−2; before and after the diapir outcrop, respectively) from 2011 to 2022 were provided by the Ebro Water Authority (CHE, 2023a and b) and the Navarra Geographic Center (SITNA, 2023). The estimated discharge of the Longinos spring was calculated by the dilution method from the electrical conductivity and discharge of the Ega river (Table 1, supplementary material).

The cave topography, position and elevation of the main clastic deposits respecting the cave entrance were conducted using a DistoX2 Leica (x310) modified with an electronic base plate to measure the direction and dip between selected points in the cave (Heeb, 2014). The data were processed with the VisualTopo software (https://vtopo.free.fr/) and was validated with the topographic maps produced by Eraso (1959) and Chasco (2021). The morphological features were described following criteria by Ford and Williams (2007). The temperature, pH and electrical conductivity of the Longinos cave spring were measured in situ using a Thermo Orion 250A portable pH-meter with temperature compensation and a conductivimeter Jenway 4200 with automatic correction of temperature. The chemical analysis of the water was conducted by the Geochemistry Laboratory of the Earth Sciences Department at the University of Zaragoza. The speciation–solubility calculations have been performed with the PHREEQC code (Parkhurst and Appelo, 2013) and the PITZER thermodynamic database included in the PHREEQC package. Two detrital sequences (dep 1 and 2) were identified and described following Miall facies codes (1996). Finally, three charcoal fragments were recovered from deposits 1 and 2 (dep 1: samples U4 and U27; dep 2: sample U5) for accelerator mass spectroscopy (AMS) ^{14}C dating (Table 2, supplementary material). Radiocarbon ages were calibrated using in Clam 2.2 package (Blaauw, 2010) running in r (R Development Core Team, 2020) by using INTCAL 20 calibration curve (Reimer et al., 2020).

Table 1
Main morphometric parameters of the caprock collapse sinkholes in the upthrown block.

Parameter	Maximum	Minimum	Average	Standard deviation
Major axis (m)	1061	5	123	167,5
Elongation ratio	0,96	0,63	0,85	0,08
Area (m^2)	538,058	56	19,000	68737,04
Perimeter (m)	3241	28	344	487,77
Circularity ratio	0,98	0,47	0,90	0,10
Volume (m^3)	523,750	17	21,871	76834,39
Depth (m)	87	2	15	14,24
ANN = 0.97	z-Score = -0.35		p-value = 0,72	

4. Results

4.1. Morphosedimentary features of the Estella diapir

The diapir top can be divided into two different domains separated by a fault that forms a well-defined, up to 70 m high, 4.5 km-long, E-W trending fault scarp attributed to the uplift of the diapir and whose throw progressively decreases to the west and east (Figs. 2 and 4A). The impact of subsidence and salt upwelling significantly varies at both sites of the fault scarp. In the downthrown block located to the south, the pediment deposits that partially cover the diapir residue, are thickened due to subsidence. In contrast, the upthrown block, located to the north, shows stratigraphic anomalies related to both processes (subsidence and diapir growth). Here, the karstification of the gypsiferous caprock accounts for the formation of sinkholes and the local thickening of terraces while diapirism is responsible for the displacement of the Quaternary deposits, the disruption of the drainage system, the anomalous longitudinal profile of the Ega river and the Ega river channel migration.

4.2. Fluvial terraces, pediments levels and chronology

The Ebro river represents the regional base level and consequently, the distribution of fluvial terraces along its tributaries including the Ega river is related to repeated base-level drops and knickpoint retreat induced by the Ebro river erosion phases from the Early Pleistocene (Benito-Calvo et al., 2022). In the case of the Ega river, these downcutting-filling phases has led to a stepped sequence of 8 rock-cut terrace levels preserved in longitudinally erosional remnants along the valley from T1 to T8. However, terraces T1 to T3 (Fig. 3; upper terraces) are limited to its lowermost stretch downstream the study area at the confluence with the Ebro river (Lenaroz, 1993). This geomorphological configuration is in agreement with many other field studies (Bishop et al., 2005; Crosby and Whipple, 2006; Marrucci et al., 2018) where the number of terrace levels often decreases progressively upstream from the confluence to the source area. Based on LiDAR DEM data, the height

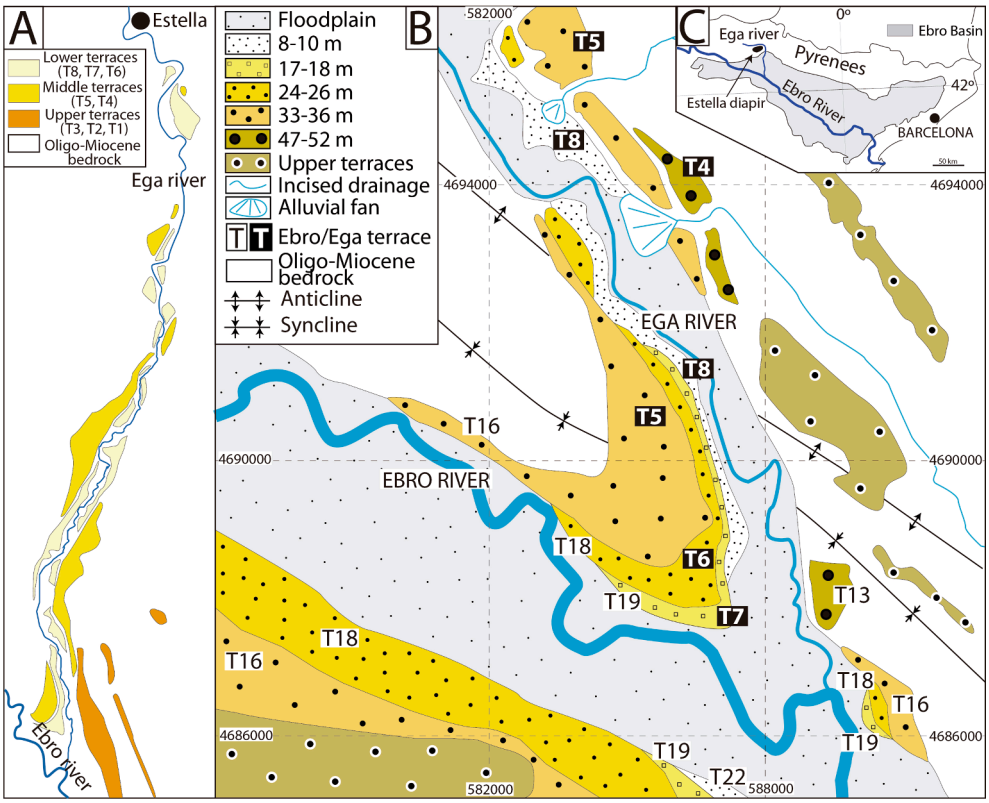

Fig. 3. (A) Simplified scheme of the spatial distribution of the Ega terraces from its confluence with the Ebro river to Estella village (Modified from Lenaroz, 1993). (B) Detailed map of the Ega and Ebro terraces at their confluence displaying the spatial correlation of the lower and middle terraces. (C) Map of the northeast of Spain showing the location of the Ebro Basin and the Ebro and Ega rivers.

of the river terraces above the channel in the study area are: T4: 47–52 m; T5: 33–36 m; T6: 24–26 m; T7: 16–17 and T8: 8–10 m. With the exception of the floodplain that consists mainly of fine-grained sediments, the terraces are constituted by 2–4 m of massive, horizontal and cross-bedded, clast-supported, sub-rounded, mainly limestone gravels embedded in a sandy matrix (Gm, Gh and GP Miall's (1978) facies) with an increasing tendency of cementation from the lower to the upper terraces. T8 terrace deposits show little pedogenic carbonate accumulation, T7 and T6 consist of very well-cemented gravels with continuous coated pebbles and T5 and T4 are made up of fully cemented gravels with massive accumulations of carbonate within the clasts.

The development of detailed geomorphological maps of the Ebro (Lenaroz, 1993; Benito-Calvo et al., 2020) and Ega rivers valleys (Lenaroz, 1993; Olive et al., 2010a,b) allow fluvial terrace correlation. At the confluence of both rivers, terraces T7, T6 and T5 of the Ega river merge with terraces T19, T18 and T16 of the Ebro river, respectively, establishing a direct spatial correlation. Besides, T8 and T4 terraces of the Ega river can be correlated with terraces T22 and T13 of the Ebro river based on their relative altitude above their present channels at their confluence (Fig. 3).

The chronology of the Ega river terraces can be estimated from their correlation with the Ebro terraces whose temporal evolution has been recently studied in detail. Based on a thorough field survey and the interpretation of aerial photographs and Digital Elevation Models derived from LiDAR data, Benito-Calvo et al. (2022) recognise a sequence of 22 fluvial rock-cut terraces in the Upper Ebro River ranging from 200 to 4 m above the present channel. The Electron Spin Resonance (ESR) dates of terraces T3 (+166 m; 1186 ± 46 ka), T10 (+80–85 m; 945 ± 118 ka), T12 (+60–65 m; 716 ± 71 ka), T15 (+37–43; 660 ± 75), T16 (+33–36 m; 630 ± 59 and 644 ± 81 ka) and T19 (+17–22 m; 387 ± 45 ka) (Benito-Calvo et al., 2022) and Optically Stimulated Luminescence (OSL) ages of T22 (+4–10 m; 22.4 ± 1.3, 24.5 ± 1.9 ka, 34.6 ± 4.3, 47.2 ± 4.7) (Benito-Calvo et al., 2022; Perucha et al., 2015) provide a strong chronological framework. The ages of the undated Ebro river terraces were estimated by Benito-Calvo et al. (2022) using a statistical regression curve and algebraic functions (Cunha et al., 2019; Benito- Calvo et al., 2020).

Based on the spatial and altitudinal correlation of the Ega and Ebro rivers terraces at their confluence (Fig. 3B) and considering the maximum and minimum ages for every terrace, the formation of the Ega river terraces was between 21 and 51 ka (36 ± 15) for T8, 342 and 432 (387 ± 45) for T7, and 563 and 725 ka (644 ± 81) for T5. The modelled ages for T6 and T4 would be around 432 and 738 ka, respectively (Benito-Calvo et al., 2022). These ages are in agreement with their pedogenic accumulation of carbonate.

Four mantled pediment levels connected to some of the terraces have been mapped in the studied area (P4, P5, P6, P8). Besides, there are other older pediment surfaces high above the terrace levels that were deposited before the entrenchment of the Ega river system (Lenaroz, 1993). Overall, pediments form extensive surfaces dissected by alluvium-infilled drainages coming from Cretaceous limestone platforms and Tertiary conglomerates and sandstone outcrops at the northern, southern and eastern edges of the Ega valley, respectively. They are made up of alternating matrix-supported limestone gravels and massive to horizontally-laminated brown silts with a total thickness between 2 and 4 m (Olive et al., 2010a,b) except for P5 pediment whose deposits thickens in the southern flank of the diapir. Here, groundwater wells for irrigation penetrate more than 43 m of alternating gravels, sands and clays without reaching the underlying tertiary bedrock (CHE, 2023a). This thickened fill also shows a conspicuous change in its sedimentology with a much higher proportion of fine-grained sediments.

4.3. Quaternary diapirism

Parallel to the strike of the Cretaceous rocks-Triassic diapir contact, the relative height of alluvium surfaces ascribed to terraces T4, T6 and T8 may change substantially due to a differential diapiric uplift (Fig. 2, see location of uplifted terraces). The rise of the terraces is maximum at the centre of the uplifted block upstream the Urederra confluence and decreases to the west and east towards the diapir edges in agreement with the throw of the fault scarp that is also maximum at its middle section. At Estella village, T8 tread is arched 6 m at the base of the fluvial scarp. Upstream the confluence with the Urederra river, close to the gauging station EGA-1, T6 and T8 straths are vertically displaced 12 m projecting from 24 to 36 and 10 to 22 m above the present channel, respectively. Further upstream, close to the end of the diapiric edge, T6 tread is also arched 7 m. Finally, a highly-cemented gravel deposit situated 85 m above the present channel and hanged with respect to P5 has been ascribed to terrace T4. Considering the relative height of this level between 47 and 52 m, the displacement related to salt diapirism would be around 33–38 m (Fig. 2). The deformation recorded on the fluvial deposits also causes several anomalies in the longitudinal profile of the Ega river. The profiles of terraces T4, T6 and T8 show a sudden rise in those reaches carved in the salt stock leading to anomalous convex geometries attributed to diapir growth (Fig. 5A). T4 terrace displays a higher displacement and a strong convexity than the lower terraces that is attributed to the higher impact of diapir uplift due to its older age. However, the offset of T6 and T8 terraces is similar evidencing a discontinuous supply of salt into the diapir over time. Terraces T5 and T7 are not preserved upstream the diapir outcrop. Probably, their erosion might be associated to a period of enhanced river downcutting and scarp retreat probably due to salt upwelling. Today, the floodplain shows a steepened profile changing from a slope of 0.2 to 0.41% (Fig. 5A) when it crosses the diapir. This slope increase seems to point to the current growing activity of the Estella diapir.

The pediment correlative to P5 also shows conspicuous features associated with salt upwelling. The fault scarp attributed to the uplift of the diapir is responsible for the offset and fragmentation of this pediment surface (Fig. 4A) that once covered all the diapir top reaching the Ega river (Urabayen and Chasco, 2001). Today, only some P5 remnants are still preserved from erosion on the uplifted block. However, a thin mantle of gravels and pebbles still covers most of the salt outcrop supporting their previous extension up to the Ega river. Considering the present dip of 6° of the pediment surface out of the salt plug as the original angle of deposition, the maximum vertical displacement required to restore P5 remnants to its original location is around 40 m (Fig. 5B).

The drainage network in the Estella diapir also displays several anomalies attributable to differential vertical deformation related to salt flow. Firstly, the Ega river surrounds the Estella diapir changing in its direction from east-west before reaching the Triassic evaporites to northeast up to the Urederra confluence and finally to the south (Fig. 2). This flowing trace suggests that salt upwelling is favouring the continuous lateral migration of the river away from the diapir. This idea is supported by the formation of a prominent, subvertical fluvial scarp of up to 80 m high on the right margin of the river along the northern and eastern diapir flanks at the contact with Cretaceous marls. Regarding the scarp age, the occurrence of T4 deposits on top of it dates its initial development after T4. Since then, the scarp has continued retreating due to river undermining in those reaches where the river channel is located at the toe of the scarp. This process has led to hanging valleys and unstable slopes affected by rockfalls and landslides that threaten Estella village (Fig. 5C). Secondly, the growth of the diapir and the development of the fault scarp has generated a barrier for those consequent, north-flowing, alluvium-infilled drainages that used to traverse the diapir flowing through P5 deposits and discharging into the Ega river. At the present time, only those located at the margins of the salt outcrop where the vertical uplift is lower or those that show higher erosion rates

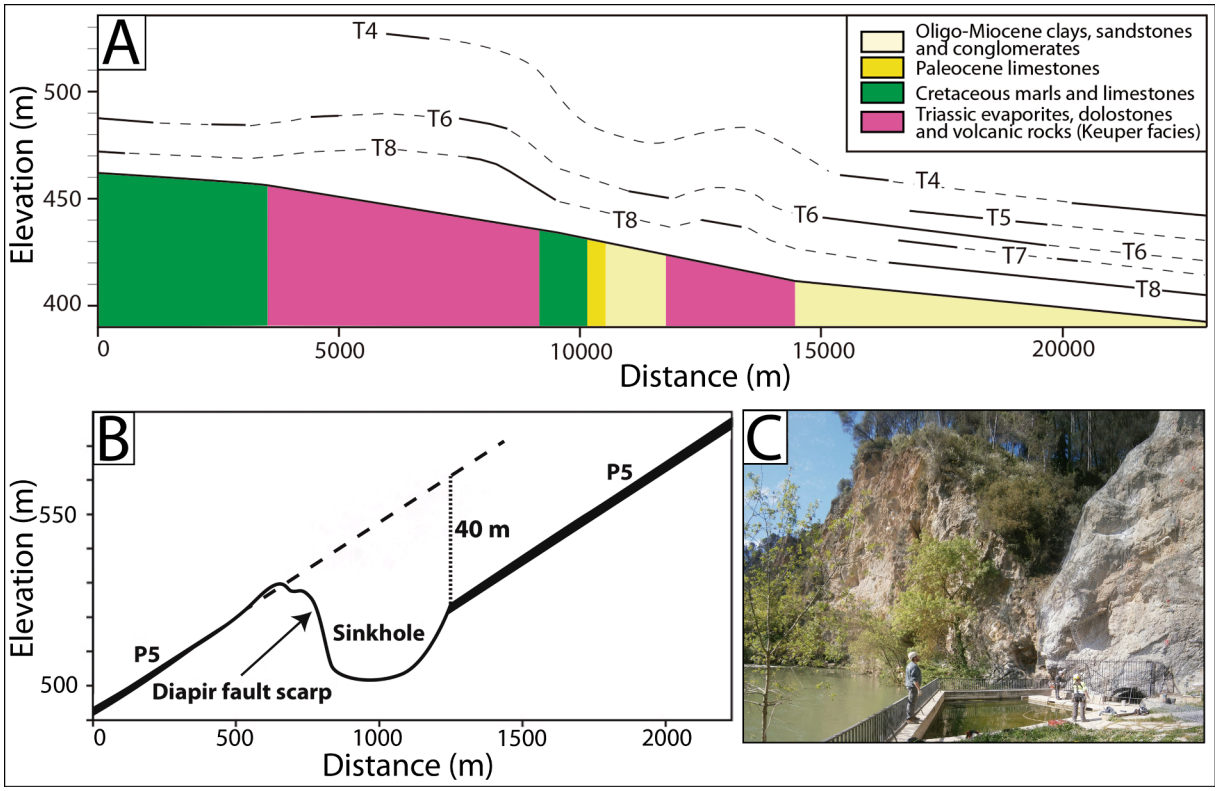

Fig. 5. A) Longitudinal profile of the Ega river (all the reach included in Fig. 2). B) P5 longitudinal profile and vertical throw at the diapir fault scarp 300 m to the east of Iguzquiza sinkhole. C) Lower passage entrance of the Longinos cave at the toe of the fluvial escarpment and saline recreational pools at Estella village. A steel fence is being installed to prevent rockfall damage to customers.

are able to flow across the fault scarp. In contrast, most of them can't keep pace with the diapir growing rate and are either defeated leading to wind gaps in the upthrown block (Fig. 4B) or deflected such as Ayegui creek that shows a sharp eastward deflection at the base of the fault scarp to flow parallel to the diapir edges (Fig. 2). The maximum difference in elevation between the top and bottom of the defeated infilled-drainages at both sides of the fault scarp is between 37 and 40 m which is in agreement with the maximum estimated offset of P5 and can be considered a rough estimate of the maximum vertical deformation subsequent to the abandonment of these infilled-fluvial drainages (Fig. 2). The minimum elevation difference is around 12 m and corresponds to a drainage carved into the central part of P5 that, before being truncated, was able to traverse the fault scarp towards the Ega river to form a large alluvial fan overlying T6 deposits (Fig. 2). The vertical displacement of this alluvium-infilled drainage at the fault scarp coincides with the 12 m uplift of its fan deposits and T6 and T8 terrace surfaces in the upthrown block suggesting that it was probably defeated after T8 formation.

4.4. *Dissolution phenomena and the Longinos cave*

The increase in the hydraulic gradient caused by diapirism in the uplifted block has favoured water infiltration, the underground karstification of the caprock and sinkhole development. The contact between the gypsiferous residue and the fluvial mantle displays an irregular geometry due to the differential dissolution of the rockhead (Fig. 6). Locally, terrace deposits are thickened reaching more than 20 m thick. In these areas, the thickened alluvium is constituted by a large proportion of overbank sands and silts that show a centripetal dipping, thicken towards the core and their dip decreases from the base to the top. This stratigraphic arrangement is interpreted to be the result of the syndepositional filling of large paleosinkholes (Fig. 6).

The karstic residue, fluvial terraces and pediments are affected by a total of 3 large compound depressions with nested collapse sinkholes of up to several tens of meter in diameter and 65 caprock collapse sinkholes. The first ones are located at the toe of fault scarp where the accumulation of water from defeated alluvium-infilled drainages

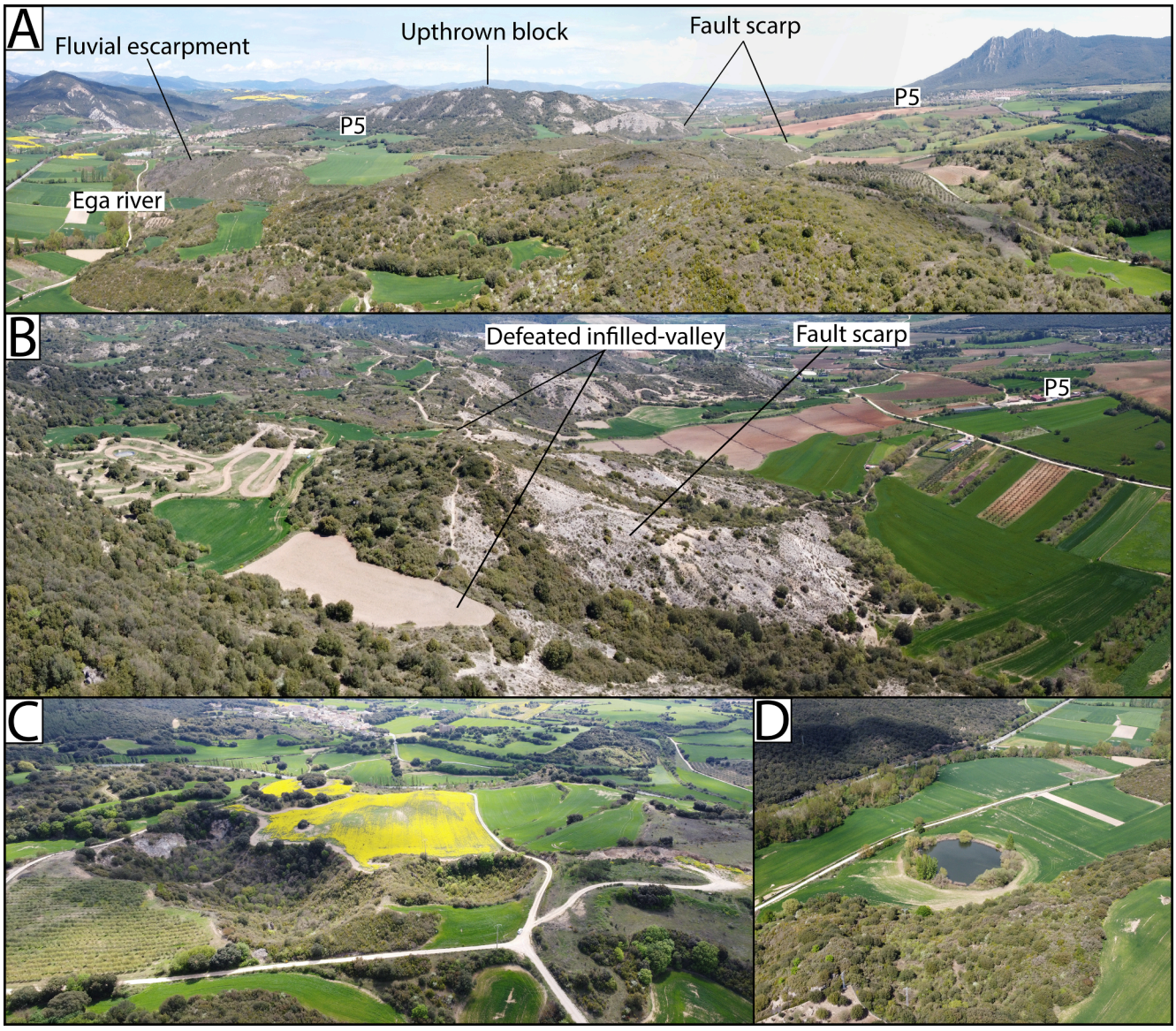

Fig. 4. (A) Panoramic view of the Estella diapir showing the offset of P5, the location of the fault scarp and the positive relief of the upthrown block eroded by the Ega river. Vertical-dipping beds of Tertiary rocks at the background. (B) Zoom of the diapir fault scarp showing defeated infilled-valleys that used to drain P5 deposits. (C) Iguzquiza compound depression formed by the coalescence of 4 collapse sinkholes. (D) Circular, collapse Arbeiza sinkhole developed in the Ega river floodplain. The bottom of the depression lies at the same elevation as the adjacent river and hosts a permanent lake.

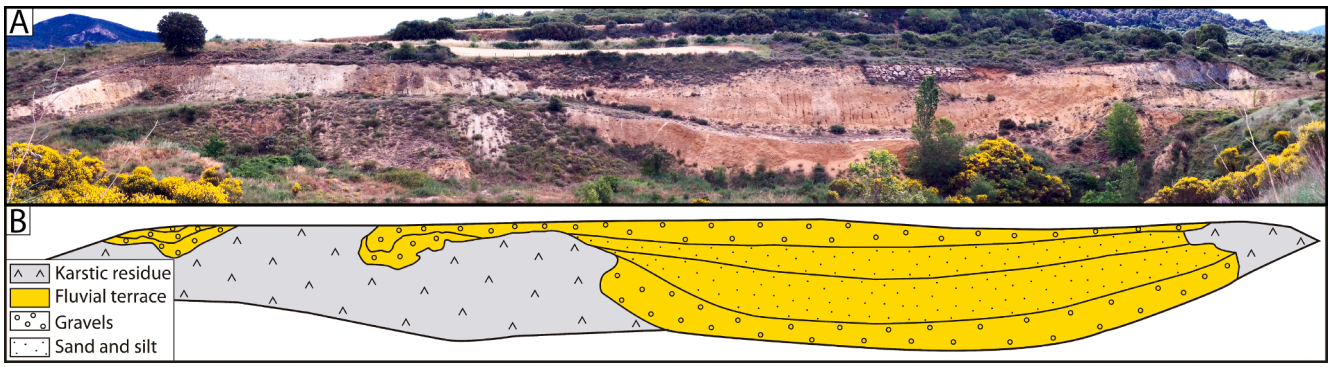

Fig. 6. Picture (A) and sketch (B) of a paleosinkhole filled by a large proportion of fine-grained sediments ascribed to T6 terrace. Note the irregular contact between the alluvial and the dissolution residue.

favours karst processes and the development of irregular-shaped closed-depressions with aerial surfaces of up to 0.5 km^2 that result from the coalescence of several smaller sinkholes. The second ones occur in the upthrown block and display a wide range of morphologies and dimensions. The major axis, area and volume varies from 1,061 to 5 m, 538,058 to 56 m^2 and 523,750 to 17 m^3, respectively (Table 1). They are normally subcircular with an average elongation ratio of 0.85 although they may occasionally show an irregular shape due to sinkhole coalescence leading to minimum elongation and circularity ratios of 0.63 and 0.47. The orientation of the major axis of the depressions shows prevalent WNW-ESE and ENE-WSW trends (Fig. 7A). In general, these closed-depressions often show well-defined scarped edges, a fresh-looking appearance and depths over 10 m with an average of 15 m (Table 1). Iguzquiza compound depression, formed by the coalescence of 4 collapse sinkholes in the 1850 is the deepest sinkhole with its 87 m deep (Urabayen and Chasco, 2001) (Figs. 2 and 4C). Except for those sinkholes located in the floodplain that intercept the phreatic level and host permanent lakes like Arbeiza sinkhole (Fig. 4D), the rest act as ponors that disrupt the local drainage and become the main entrance of runoff into the endokarst developed in the brecciated karstic residue. The visual inspection of the geomorphological map reveals a dispersed distribution that is supported by a Nearest Neighbour Index of 0.97, very close to a value of 1 that would indicate a perfect random distribution. Considering the outcropping aerial surface of the Triassic rocks, the total area affected by sinkholes is 1.4 km^2 (9.3 % of the diapir outcrop) that yields a density of 5.1 sinkholes/km^2.

The length of the major axis and the cumulative frequency has been plotted in a semi-logarithmic graph to determine the number of sinkholes that equals or exceed a particular size (Fig. 7B). The data shows a sigmoidal pattern with a high R-square value (R^2 = 0.92) by a logarithmic function although with a slight deviation for the extreme-size values of the distribution. The regression that is similar to the sinkhole pattern of other salt diapirs (Gutiérrez and Lizaga, 2016), predicts a higher probability of occurrence for sinkholes smaller than 12 m and a lower one for those larger than 350 m.

Only three vadose, 4 to 15 m long, dissolution-enlarged joints and a larger phreatic cave, named as the Longinos cave, had been described so far (Eraso, 1959; Urabayen and Chasco, 2001). The Longinos cave is located on the eastern flank of the diapir at the village of Estella (Figs. 2 and 8). It shows two, E-W oriented epiphreatic levels connected by a meandering conduit that runs parallel to the Ega river and the fluvial gypsum scarp. The cave entrance, located 8.5 m above Ega river flood plain, corresponds with the upper level, which acts as an overflow conduit (trop-plein). The 18 m long, upper level is an old epiphreatic conduit with an inward inclination from its entrance. This gallery ends when the passage becomes subhorizontal. The altitude difference between the entrance and its end is 6 m. Its altitudinal position coincides with a steady water-table related to the position of the fluvial network during T2 Ega river terrace (Urabayen and Chasco, 2001). The lower conduit consists of a 15 m long, 3 m high and flat ceiling room with large

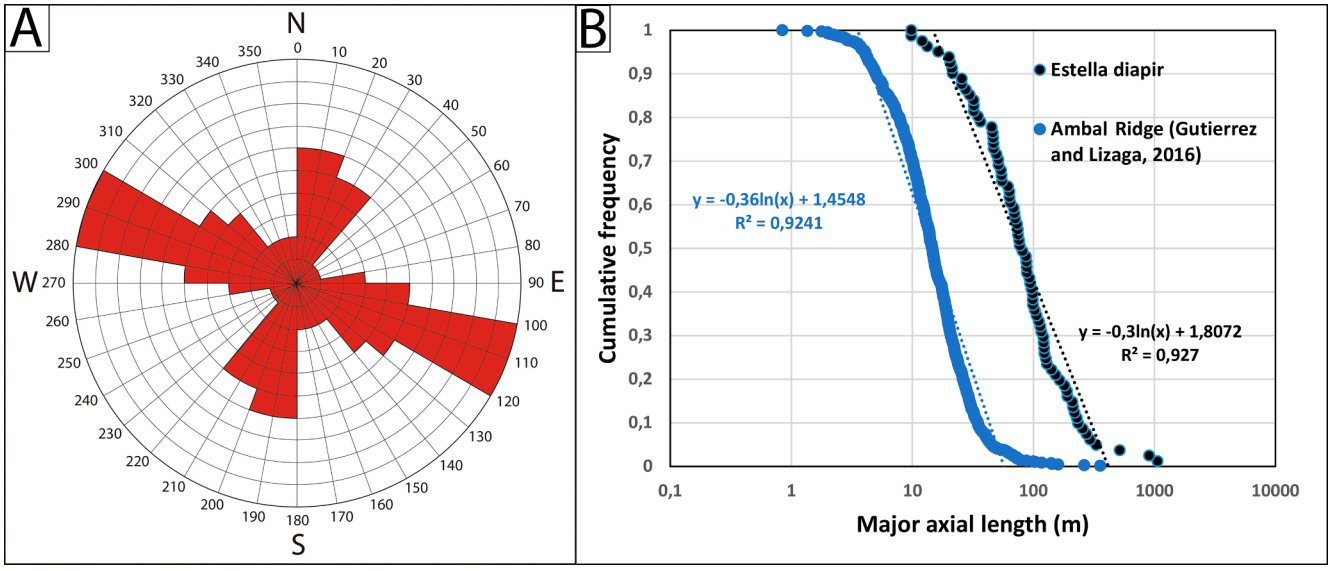

Fig. 7. A) Rose diagram showing the orientation of sinkholes major axis considering intervals of 10°. B) Semi-log graphs of cumulative frequency versus major axial length of the closed depressions, and logarithmic regressions functions (dashed lines) in the Estella and Ambar Ridge diapirs.

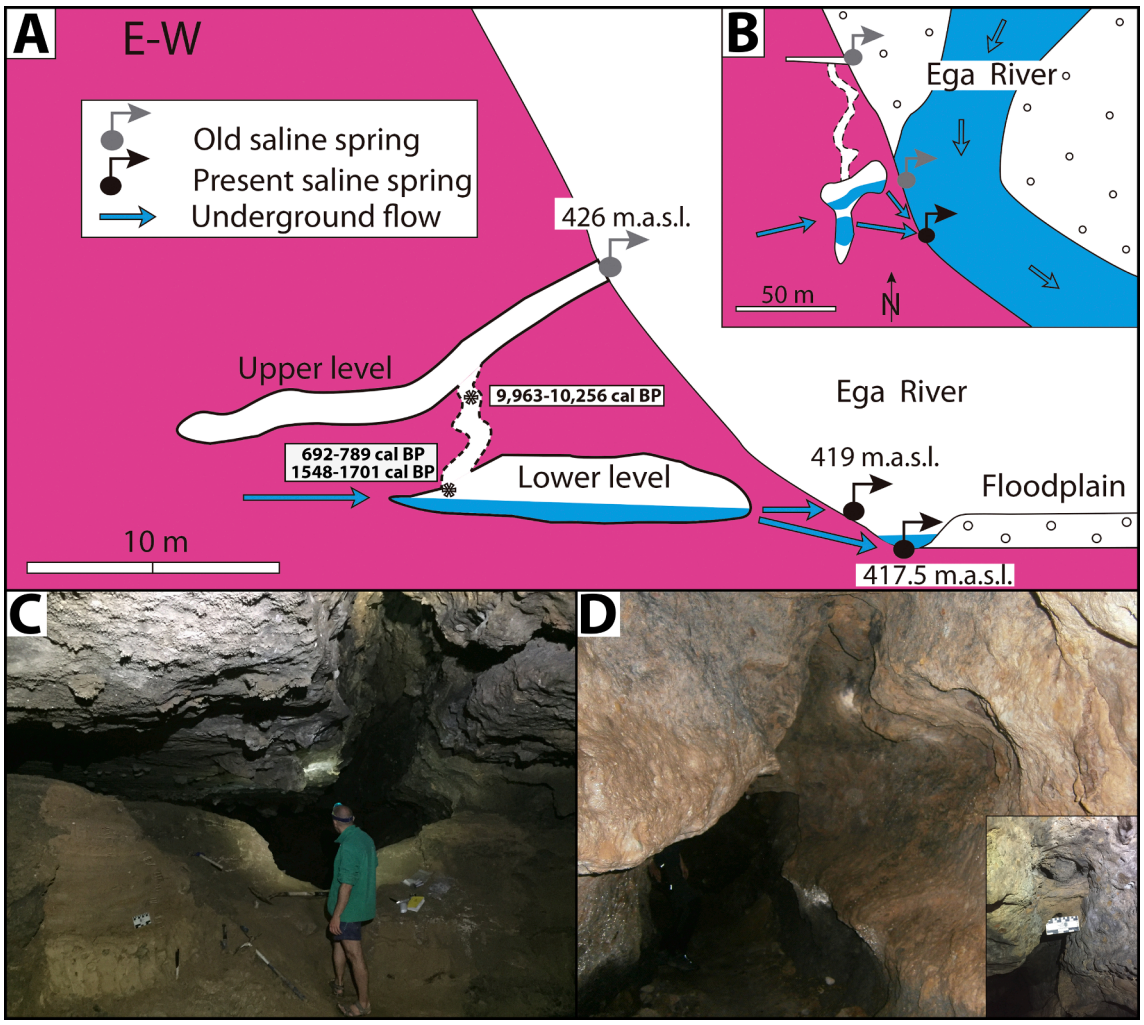

Fig. 8. Profile (A) and plan view (B) of the Longinos cave showing the flow-path of the saline water and abandoned and present springs (the vertical and horizontal scales are the same). Antigravitative erosion morphologies include a flat ceiling and pendants of gypsum blocks (C), a ceiling channel (D, detail of the filling in lower corner) and wall notches (D).

gypsum blocks that protrude as pendants and a sinuous channel carved into the ceiling (Fig. 8C). These morphologies have been related to an antigravitative erosion process in response to sediment accumulation on the floor (Lauritzen and Lauritsen, 1995; Farrant and Smart 2011; Cooper and Covington, 2020). Two charcoal samples located at the base and top of the alluvial sequence, yielded calibrated radiocarbon ages of 1548–1701 and 692–789 cal BP, respectively (Fig. 2, Table 2, supplementary material). The meandering conduit that connects both levels, also shows antigravitative erosion morphologies including wall notches and a meandering ceiling channel (Fig. 8D). The filling of the ceiling channel is still preserved in some sections suggesting that the cave was completely filled during this antigravitational stage. A charcoal sample collected in a blind area from a sandy deposit at 0.5 m below the ceiling provides a radiocarbon age of 9,963–10,256 cal BP (Fig. 2, supplementary material). The antigravitative morphologies of the lower level and the meandering conduit, the radiocarbon ages and the cut and fill geometry of the Longinos cave deposits point to successive aggradation-incision stages related to intermittent close-open conditions of the cave outlet.

4.5. Hydrology of the Estella diapir

Runoff in the diapir outcrop is limited and surface water quickly seeps through sinkholes and flows along underground karstic conduits to finally recharge the underlying evaporitic endokarst system. The Longinos spring represents the main groundwater drainage system of the diapir aquifer (Chemical balance of the Ega river, supplementary material). It consists of two discharge points located at different heights at the base of the fluvial scarp and connected to a perennial saline stream that flows into the main room of the lower conduit of the Longinos Cave to form a large pool. The lower spring comes up to the surface at the bottom of the Ega river, which represents the hydrological base level, with an average discharge of around 80 l/s (Table 1, supplementary material). The upper one is situated 1.5 m above the present channel coinciding with the floodplain tread and works as an overflow conduit (trop-plein) today.

The water samples are sodium chloride - calcium sulphate type and are undersaturated with respect to calcite, dolomite, gypsum and anhydrite and very far from the equilibrium with respect to halite determined by the PHREEQC model (Parkhurst and Appelo, 2013). This chemical composition is consistent with the dissolution of carbonates and sulphates predominant in the caprock. The TDS and electrical conductivity of this saline water ranges from 6192 to 8658 mg/l and from 7590 to 12368 μs/cm, respectively, with increasing values as the discharge decreases (CHE, 2019; SITNA, 2023; Table 2, supplementary material). Considering its average discharge and TDS, the estimated salt flux of the Longinos spring into the Ega river would be roughly 48 tons/day accounting (on average) for 70 % increase in the electrical

conductivity of the Ega river across the diapir (from 538 to 888 μs/cm; Table 1, supplementary material). The saline water shows a constant pH of 6.9–7.1 and a temperature ranging from 15.4 to 18,9 °C throughout the year that is similar to the average temperature of the study area and suggests a shallow flow path within the thick karstic residue, which is almost devoid of halite. The load of *Escherichia coli* and *Enterococcus* spp. that has linearly increased since 2014 reaching over 400 ufc/100 ml in response to farming activities on the pediment P5 (CHE, 2019), locates its main recharge area in the downthrown block. Water from rainfall and runoff seeps into P5 deposits and flows at the contact with the dissolution residue until reaching the closed-depressions located at the base of the fault scarp. Once here, groundwater sinks into dissolutional conduits developed in the caprock towards the Longinos cave and the Ega river across the fault scarp (Fig. 2).

5. Discussion

5.1. The evolution and uplift rate of the Estella diapir

The evolution and uplift rate of the Estella diapir can be unravelled considering the vertical displacement of the Ega terraces and pediments and their correlated ESR and OSL ages (Perucha et al., 2015; Benito-Calvo et al., 2022). The similar offset of T4, P5 and infilled valleys draining P5 suggests that diapir uplift started after P5/T5 formation. In addition, the equal vertical displacement of terraces T8 and T6 upstream Estella village clearly evidences that diapir growth was negligible between the sedimentation of these two terraces. These geological data support a minimum of two growing events separated by a period of inactivity. The first growing episode started with the beginning of diapirism after T5 at around 644 ± 81 ka and stopped before T6 at around 432 ka. Salt motion caused the development of the fault scarp, the rupture of P5, the offset of T4 and the cut-off of those alluvium-infilled drainages that used to traverse the salt outcrop. Diapir uplift enhanced river erosion and incision that came into the development of a prominent fluvial scarp carved at the diapir edges and the erosion of T5 deposits upstream Estella village. Subtracting the vertical displacement of T8 (12 m) to the total offset recorded in T5/P5 deposits (40 m), the minimum vertical deformation during this first halokinetic event would be 28 m (40–12 m) for a time span of around 212 ± 81 ka that yields an uplift rate of around 0.09–0.21 mm/yr. Later, between T6 and T8, the salt diapir underwent a long period of quiescence and some infilled drainages were able to cut across the fault scarp to form extensive alluvial fans at the north side of the salt diapir on top of T6 terrace deposits. The second growing event happened after T8 formation at around 36 ± 15 ka. Throughout this period, T6 and T8 were arched and uplifted a maximum of 12 m in agreement with the vertical displacement of those infilled-valleys that previously pierced the fault scarp and were finally defeated leading to wind gaps. Several geomorphological evidences suggest that this growing episode continues today. Firstly, the steepening of the present floodplain from 0.2 to 0.4 % and secondly, the occurrence of triangular facets and hanging valleys along the fluvial scarp due to a rapid scarp retreat and river incision probably in response to salt upwelling. This idea is supported by the adjustment of the Longinos cave karstic system in the last 800 years. According to historical data (Hermoso de Mendoza, 2007) the Longinos upper spring that works today as a top-plein held most of the discharge during the XII century, only half in 1950 and almost none today recording its progressive abandonment in favour of the lower spring in response to the continuous incision of the Ega river probably due to diapir uplift. Assuming the diapir is still growing today, the uplift rate of this second upwelling event would be 0.23–0.57 mm/yr decreasing to half at the diapir edges. This value doubles the one recorded during the first growing phase. Considering the age and total displacement of T5/P5 deposits and infilled valleys since the beginning of the uplift, the long-term, average growing rate of the Estella diapir would be 0.05–0.07 mm/yr. The existence of a calm period between two upwelling events of different ratios demonstrate the episodic kinematic of the Estella diapir in agreement with the history of most salt domes that includes growing pulses interrupted by long periods of inactivity (Millán, 2004; Hudec and Jackson, 2011, Harding and Huuse, 2015).

5.2. Triggering mechanism of diapirism

Numerous studies demonstrate that salt flowage towards the river valleys in response to erosion-induced differential loading causes terrace tilting and arching, oversteepened slopes and cave abandonment (Lucha et al., 2012; Bruthans et al., 2010; Guerrero, 2017; Gutiérrez et al., 2014, 2019 and references therein). In the Estella diapir, several lines of evidence suggest that differential unloading caused by the Ega river incision seems to be the only possible triggering mechanism for salt migration and diapirism. Firstly, the Pamplona fault, the South Pyrenean Frontal thrust and the Oco and Learza faults (Fig. 1) lack any evidence of recent surface displacement. Secondly, the seismic catalog of the IGN does not record any earthquake attributable to these basement faults since the beginning of the data collection in 1370 suggesting that the area seems to be tectonically inactive. Finally, GPS measurements of deformation across the range suggest that the Pyrenees continues today under an extensive tectonic regime in response to the separation of the European and Iberian plates at a rate between 0.2 and 0.5 mm/yr across the 150 km wide range (Asensio et al., 2012; Rigo et al., 2016) whereas the Estella diapir growth rate alone equals this value supporting a nontectonic genesis. On the other hand, the Ega river has excavated a deep valley carved into the Cretaceous-Triassic diapir contact, locally entrenched 500 m below the surrounding bedrock reliefs. Moreover, based on subsurface data (IGME, 1990a,b; Camara et al., 2020): (1) Triassic salt is far from being exhausted and its thickness still ranges between 1000 and 3000 m with an average value of around 1500–2000 m, and (2) the overburden on top of the Triassic bedrock around the Estella diapir is over 3 km thick and exerts a strong lithostratigraphic pressure on the salt. This overburden load together with the topographic difference between the valley and the surrounding reliefs create a significant hydraulic head gradient towards the valley that might enhance salt flow. This genetic hypothesis is in agreement with the deformation recorded on the terrace and pediment levels whose uplift rates yield a direct relationship with river erosion. Considering the average height of the terraces above the present river channel and the correlated ages of the Ega terraces (Lenaroz, 1993; Perucha et al., 2015; Benito-Calvo et al. 2022), the river incision rates during the first halokinetic event, the quiescence phase and the latest upwelling event are around 0.05, 0.03 and 0.2 mm/yr, respectively. These values show the same trend as halokinesis with a moderate downcutting period during the beginning of diapirism, followed by a lower erosion phase that coincides with the quiescence stage and a much higher incision value since T8 when the growing rate is maximum. Finally, the anomalous thickness of P5 deposits on the downthrown block reaching more than 43 m is related to either salt dissolution or salt-withdrawal subsidence. The lack of sinkholes affecting the large pediment surface points to the migration of salt as the main responsible phenomena of its thickening and suggests that the downthrown block represents the main feeding area of the upthrown block. This is congruent with a north- northeast flow of salt towards areas unloaded by the Ega river erosion.

5.3. The geomorphologic response to diapirism

The large number of collapse sinkholes in the upthrown block, the development of large depressions at the toe of the fault scarp, the existence of caves developed in the gypsiferous caprock and the increase in water salinity of the Ega river evidence that the karstification phenomenon happens simultaneously to diapirism as it has already been reported in other salt diapirs (Talbot and Aftabi, 2004; Bruthans et al., 2006, 2010; Gutiérrez and Lizaga, 2016, Guerrero et al., 2019). High-pixel resolution orthoimages and LiDAR data allow calculating

sinkhole parameters with great accuracy and comparing their frequency-size distribution with other salt diapir datasets. A similar regression generated with the major axis of sinkholes in Ambal Ridge salt diapir in the Zagros Mountain in Iran (Gutiérrez and Lizaga, 2016), also displays a symmetric sigmoidal curve to the one obtained for the Estella diapir with a high logarithmic correlation ($R^2 = 0.92$) and a low deviation between the empirical data and the regressions for extreme-size values (Fig. 7B). However, the size-distribution sinkhole dataset of the Iranian diapir is displaced to the origin of the graph one order of magnitude. This difference means that the depressions of the Estella diapir show larger dimensions than those of Ambal Ridge. Two main factors may explain the higher formation probability of a large sinkhole in the Estella Diapir: (1) the higher average rainfall rate of the study area (750 mm/year; Urabayen and Chasco, 2001) which doubles the one recorded in Ambal Ridge (365 mm/yr; Jalali et al., 2019) and favours dissolution processes, and (2) a thicker and highly-cemented dissolution residue with a higher mechanical strength on top of the Estella diapir that allows the development of larger underground voids before their roof collapse (Guerrero et al., 2015). In addition, the major axis of the sinkholes shows prevalent WNW-ESE and ENE-WSW (Fig. 7A) orientations that match with the strike of the primary faults (Olive et al., 2010a, b) and the elongation of the salt diapir suggesting that the structure is controlling the development of the depressions. Regarding the endokarst, although the large number of sinkholes with a random distribution suggests the existence of a well-developed subsurface karst conduit network developed in the thick insoluble residue, the Longinos cave is the only known underground system in the Estella diapir. Nevertheless, local farmers and previous studies (Eraso, 1957) report that during high intensity rainfall events, as the Iguzquiza sinkhole progressively fills up and drains, the Arbeiza sinkhole overflows providing a good indicator for their underground hydraulic connection through ascending phreatic passages. Despite the existence of other inaccessible endokarstic conduits, the chemical balance of the Ega river since 2011 (Table 1, supplementary material) supports the lack of any other permanent saline flux discharging into the river apart from the Longinos spring, which represents the main drainage system of the diapir.

Finally, the ascending trend of the Longinos cave upper level has two contrasting interpretations. Either, it represents an ascending conduit in a phreatic environment or a back-tilted passage due to diapir uplift. The existence of springs associated with ascending waters in the study area such as the previously mentioned system Iguzquiza-Arbeiza sinkholes supports the first option. Nevertheless, several evidences seem to support the diapir growth hypothesis: (1) the uplift of terrace T2 at Estella village coincides with the net back-tilting of the upper conduit (6 m of vertical difference between its entrance and its end), (2) the sub-horizontal geometry of the lower level that suggests the existence of a dense network of fissures at the diapir flank to develop a water-table cave system rather than a phreatic cave with ascending passages (Ford and Ewers, 1978), (3) the increase in the river erosion rate in the last 36 $\pm$ 15 ka and (4) the antigravitative morphologies of the lower level and meandering conduit that points to a recurrent infilling process probably favoured by the uplift of the diapir and consequently the increase in the hydraulic gradient, erosion of the topographic surface and sediment load into the cave.

6. Conclusions

The deformation recorded in the Ega river terraces and pediments, infilled-valleys and the Longinos cave evidences that karstification, salt-withdrawal subsidence and diapir uplift are coetaneous active processes. The dissolution of the gypsiferous caprock causes the development of a dense, randomly distributed sinkhole network that disrupts the drainage system and feeds a well-developed endokarst system. The Longinos Cave represents the main drainage system and holds a permanent calcium sulphate-sodium chloride saline spring that discharges into the Ega river an average of 48 tons of dissolved salt per day and contributes to its abrupt salinity increase. Salt-withdrawal subsidence is responsible for the anomalous thickness of P5 deposits to the south of the diapir fault scarp where salt flows from the downthrown block to the upthrown block in response to fluvial erosion unloading. Nevertheless, salt flow and diapir growth have not been continuous but episodic with two uplift pulses between T4 and T6 and T8 to present separated by a calm period between T6 and T8 yielding an average and maximum growing rates of 0.05–0.07 mm/yr and 0.23–0.57 mm/yr, respectively. Future geomorphological studies are needed to determine whether other salt stocks of the Cantabrian basin would be also undergoing active diapirism at similar salt upwelling rates.

Declaration of Competing Interest

The authors declare that they have no known competing financial interests or personal relationships that could have appeared to influence the work reported in this paper.

Data availability

Data will be made available on request.

Acknowledgements

The research has been funded by the Spanish national project PID2021-123189NB-I00 (Ministerio de Ciencia e Innovación).

Appendix A. Supplementary data

Supplementary data to this article can be found online at https://doi.org/10.1016/j.catena.2023.107531.

References

Abalos, B., Alkorta, A., Iribar, V., 2008. Geological and isotopic constraints on the structure of the Bilbao Anticlinorium (Basque-Cantabrian Basin, north Spain). J. Struct. Geol. 30, 1354–1367. https://doi.org/10.1016/j.jsg.2008.07.008.

Abedi, F., Amirian Chakan, A., Faraji, M., Taghizadeh, R., Kerry, R., Razmjoue, D., Scholten, T., 2021. Salt dome related soil salinity in southern Iran: Prediction and mapping with averaging machine learning models. Land Degrad. Dev. 32, 1540–1554. https://doi.org/10.1002/ldr.3811.

Adeoti, B., Webb, A., 2022. Geomorphology of contractional salt tectonics along the Kuqa fold-thrust belt, northwestern China: Testing pre-kinematic diapir versus source-fed thrust and detachment fold models. J. Struct. Geol. 161, 104638. https://doi.org/10.1016/j.jsg.2022.104638.

Almendros, M.A., Antón, F.J., 1983. El complejo kárstico-yesífero subterráneo "Pedro Fernández" (Estremera, Provincia de Madrid). Cuadernos do Laboratorio Xeolóxico de Laxe 5, 333–341.

Asensio, E., Khazaraddze, G., Echeverria, A., King, R.W., Vilajosana, I., 2012. GPS studies of active deformation in the Pyrenees. Geophys. J. Int. 190, 913–921. https://doi.org/10.1111/j.1365-246X.2012.05525.x.

Backé, G., Baines, G., Giles, D., Preiss, W., Alesci, A., 2010. Basin geometry and salt diapirs in the Flinders Ranges, South Australia: Insights gained from geologically-constrained modelling of potential field data. Mar. Pet. Geol. 27, 650–665. https://doi.org/10.1016/j.marpetgeo.2009.09.001.

Baikpour, S., Motiei, H., Najafzadeh, K., 2016. Geological and geophysical study of salt diapirs for hazardous waste disposal. IJEST 13, 1951–1972. https://doi.org/10.1007/s13762-016-1036-x.

Barnolas, A., Pujalte, V., 2004. La Cordillera Pirenaica: Definición, límites y división. In: Vera, J.A. (Ed.), Geología De España. SGE-IGME, Madrid, pp. 233–240.

Benito-Calvo, A., Arnold, L.J., Mora, R., Martínez-Moreno, J., Demuro, M., 2020. Reconstructing Mousterian landscapes in the southeastern Pyrenees (Roca dels Bous site, Pre-Pyrenees ranges, Spain). Quat. Res. 97, 167–186. https://doi.org/10.1017/qua.2020.29.

Benito-Calvo, A., Moreno, D., Fujioka, T., López, G.I., Martín-González, F., Martínez-Fernández, A., Hernando-Alonso, I., Karampaglidis, T., Bermúdez de Castro, J.M., Gutiérrez, F., 2022. Towards the steady state? A long-term river incision deceleration pattern during Pleistocene entrenchment (Upper Ebro River, Northern Spain). Glob. Planet. Change. 213, 103813. https://doi.org/10.1016/j.gloplacha.2022.103813.

Bishop, P., Hoey, T.B., Jansen, J.D., Artza, I.L., 2005. Knickpoint recession rate and catchment area: The case of uplifted rivers in Eastern Scotland. Earth Surf. Proc. Landf. 30, 767–778. https://doi.org/10.1002/esp.1191.

Blaauw, M., 2010. Methods and code for 'classical' age-modelling of radiocarbon sequences. Quat. Geochronol. 5, 512–518. https://doi.org/10.1016/j.quageo.2010.01.002.

Boubaya, D., Allek, K., Hamoudi, M., 2011. Is there a hidden near surface salt diapir in the Guelma Basin, north-east of Algeria? J. Appl. Geophys. 73, 348–356. https://doi.org/10.1016/j.jappgeo.2011.02.006.
Bruthans, J., Filippi, M., Geršl, M., Zare, M., Melková, J., Pazdur, A., Bosák, P., 2006. Holocene marine terraces on two salt diapirs in the Persian Gulf, Iran: age, depositional history and uplift rates. J. Quat. Sci. 21, 843–857. https://doi.org/10.1002/jqs.1007.
Bruthans, J., Filippi, M., Zare, M., Churackova, Z., Asadi, N., Fuchs, M., Adamovic, J., 2010. Evolution of salt diapir and karst morphology during the last glacial cycle; effects of sea-level oscillation, diapir and regional uplift and erosion (Persian Gulf, Iran). Geomorphology 121, 291–304. https://doi.org/10.1016/j.geomorph.2010.04.026.
Calaforra, J.M., Pulido-Bosch, A., 1996. Some examples of gypsum karsts and the more important gypsum caves in Spain. Int. J. Speleol 25, 225–237.
Camara, P, 2020. Inverted turtle salt anticlines in the Eastern Basque-Cantabrian basin, Spain. Mar. Pet. Geol., https://doi.org/104358. 10.1016/j.marpetgeo.2020.104358.
Chasco, A., 2021. Análisis previo para acometer una obra de emergencia en la captación en manantial del agua salada. Scientific report. Ingenieria Geológica s.l., Ayuntamiento de Estella-Lizarra, Pamplona.
CHE, 2019. Perfil Ambiental de Zona de Baño. Manantial agua salada de Estella/Lizara. Scientific report ES220C0971959. Confederación Hidrográfica del Ebro, Ministerio para la Transición Ecológica, Madrid.
CHE, 2023b. Web de consulta de la calidad de las aguas superficiales. Confederación Hidrográfica del Ebro, http://www.datossuperficiales.chebro.es:81/WCASF/ (accessed 9 May 2023).
CHE, 2023a. Geoportal SITEbro. Confederación Hidrográfica del Ebro, http://iber.chebro.es/geoportal/ (accessed 9 May 2023).
Cooper, M.P., Covington, M.D., 2020. Modeling cave cross-section evolution including sediment transport and paragenesis. Earth Surf. Proc. Landf. 45, 2588–2602. https://doi.org/10.1002/esp.4915.
Corella, J., Stefanova, V., Anjoumi, A., Rico, E., Giralt, S., Moreno, A., Montero, A., Valero-Garcés, B., 2013. A 2500-year multi-proxy reconstruction of climate change and human activities in northern Spain: The Lake Arreo record. Palaeogeogr. Palaeoclimatol. Palaeoecol. 386, 555–568. https://doi.org/10.1016/j.palaeo.2013.06.022.
Crosby, B.T., Whipple, K.X., 2006. Knickpoint initiation and distribution within fluvial networks: 236 waterfalls in the Waipaoa River, North Island, New Zealand. Geomorphology, 82, 16-38. https://doi.org/ 10.1016/j.geomorph.2005.08.023.
Cunha, P.P., Martins, A.A., Gomes, A., Stokes, M., Cabral, J., Lopes, F.C., Pereira, D., de Vicente, G., Buylaert, J.P., Murray, A.S., Antón, L., 2019. Mechanisms and age estimates of continental-scale endorheic to exorheic drainage transition: Douro river. Western Iberia. Glob. Planet. Chang. 181 https://doi.org/10.1016/j.gloplacha.2019.102985.
Dahm, T., Heimann, S., Bialowons, W., 2011. A seismological study of shallow weak micro-earthquakes in the Urban area of Hamburg city, Germany, and its possible relation to salt dissolution. Nat. Haz. 58, 1111–1134. https://doi.org/10.1007/s11069-011-9716-9.
De Ruig, M.J., 1995. Extensional diapirism in the Eastern Prebetic foldbelt, Southeastern Spain, in: Jackson, M., Roberts, D., Snelson, S. (Eds.), Salt Tectonics: a Global Perspective. AAPG Memoir 65, Tulsa, Oklahoma, pp. 353-367.
Dooley, T.P., Jackson, M.P.A., Hudec, M.R., 2009. Inflation and deflation of deeply buried salt stocks during lateral shortening. J. Struc. Geol., 31, 582-600. https://doi.org/ 10.1016/j.jsg.2009.03.013.
Dreybrodt, W., 2004. Dissolution: evaporite and carbonate rocks. In: Gunn, J. (Ed.), Encyclopedia of Caves and Karst Science. Fitzroy Dearborn, New York, pp. 295–300.
Eraso, A., 1957. Karst en yeso del diapiro de Estella. Munibe 4, 201–230.
Farrant, A., Smart, P., 2011. Role of sediment in speleogenesis; sedimentation and paragenesis. Geomorphology, 134. 79-93. https://doi.org/ 10.1016/j.geomorph.2011.06.006.
Ferrer, O., Jackson, M.P.A., Roca, E., Rubinat, M., 2012. Evolution of salt structures during extension and inversion of the Offshore Parentis Basin (Eastern Bay of Biscay). Geol. Soc. Spec. Pub. 363, 361–379. https://doi.org/10.1144/SP363.16.
Ford, D.C., Ewers, R.O., 1978. The development of limestone cave systems in the dimensions of length and depth. Can. J. Earth Sci. 15, 1783–1798. https://doi.org/10.1139/e78-186.
Ford, D.C., Williams, P., 2007. Karst hydrogeology and geomorphology. Wiley, Chichester.
Frumkin, A., 1996. Uplift rate relative to base-levels of a salt diapir (Dead Sea Basin, Israel) as indicated by cave levels. Geol. Soc. Spec. Pub. 100, 41–47. https://doi.org/10.1144/GSL.SP.1996.100.01.04.
García-Castellanos, D., Vergés, J., Gaspar-Escribano, J., Cloetingh, S., 2003. Interplay between tectonics, climate and fluvial transport during the Cenozoic evolution of the Ebro Basin (NE Iberia). J. Geophys. Res. 108, 2347. https://doi.org/10.1029/2002JB002073.
García-Mondejar, J., 1996. Plate reconstruction of the Bay of Biscay. Geology 24, 635–638. https://doi.org/10.1130/0091-7613(1996)024<0635.
Guerrero, J., 2017. Dissolution collapse of a rising diapir from radial, concentric and salt-withdrawal faults overprinting in Salinas de Oro salt plug, N Spain. Quat. Res. 87, 331–346. https://doi.org/10.1017/qua.2016.17.
Guerrero, J., Brunh, R.L., McCalpin, J., Gutiérrez, F., Willis, G., 2015. Salt-dissolution faults versus tectonic faults from the case study of salt collapse in Spanish Valley, SE Utah (USA). Lithosphere 7, 46–58. https://doi.org/10.1130/L385.1.
Guerrero, J., Desir, G., Roqué, C., Zarroca, M., Fabregat, I., 2019. The episodic rise, net growing rate and kinematics of radial faults of the Salinas de Oro diapir using paleoseismological techniques (NE Spain). Salt upwelling versus karstic subsidence. Geomorphology 342, 210–222. https://doi.org/10.1016/j.geomorph.2019.06.018.
Gutiérrez, F., Carbonel, D., Kirkham, R.M., Guerrero, J., Lucha, P., Matthews, V., 2014. Can flexural-slip faults related to evaporite dissolution generate hazardous earthquakes? The case of the Grand Hogback monocline of west-central Colorado. GSA Bull., 126, 1481-1494. https://doi.org/ 10.1130/B31054.1.
Gutiérrez, F., Lizaga, I., 2016. Sinkholes, collapse structures and large landslides in an active salt dome submerged by a reservoir. The unique case of the Ambal ridge in the Karun River, Zagros Mountains. Iran. Geomorphology 254, 88–103. https://doi.org/10.1016/j.geomorph.2015.11.020.
Gutiérrez, F., Fabregat, I., Roqué, C., Carbonel, D., Guerrero, J., García-Hermoso, F., Zarroca, M., Linares, R., 2016. Sinkholes and caves related to evaporite dissolution in a stratigraphically and structurally complex setting, Fluvia Valley, eastern Spanish Pyrenees. Geological, geomorphological and environmental implications. Geomorphology 267, 76–97. https://doi.org/10.1016/j.geomorph.2016.05.018.
Gutiérrez, F., Sevil, J., Silva, P.G., Roca, E., Escosa, F., 2019. Geomorphic and stratigraphic evidence of Quaternary diapiric activity enhanced by fluvial incision. Navarrés salt wall and graben system, SE Spain. Geomorphology 342. https://doi.org/10.1016/j.geomorph.2019.06.002.
Harding, R., Huuse, M., 2015. Salt on the move: Multi stage evolution of salt diapirs in the Netherlands North Sea. Mar. Pet. Geol. 61, 39–55. https://doi.org/10.1016/j.marpetgeo.2014.12.003.
Heeb, B., 2014. The next generation of the distox cave surveying instrument. CREG J. 88, 5–8.
Hermoso de Mendoza, J., 2007. La Playa fluvial. http://www.sasua.net/estella/articulo.asp?f=playafluvial (accessed 12 April 2023).
Hudec, M.R., Jackson, M.P.A., 2011. The salt mine: a digital atlas of salt tectonics. AAPG Memoir 99, University of Texas, Austin, Bureau of Economic Geology, Udden Book Series 5.
Hudec, M.R., Jackson, M.P.A., 2007. Terra infirma: understanding salt tectonics. Earth Sci. Rev. 82, 1–28. https://doi.org/10.1016/j.earscirev.2007.01.001.
IGME, 1990a. Documentos sobre la geología del subsuelo de España: Cantábrica. Instituto Geológico y Minero de España, VII, Madrid.
IGME, 1990b. Documentos sobre la geología del subsuelo de España: Ebro-Pirineos. Instituto Geológico y Minero de España, VI, Madrid.
IGME, 1978a. Memoria y mapa geológico 1:50.000 de la hoja de Estella (140). Instituto Geológico y Minero de España, Madrid.
Iribar, V., Abalos, B., 2011. The geochemical and isotopic record of evaporite recycling in spas and salterns of the Basque Cantabrian basin. Spain. App. Geochem. 26, 1315–1329. https://doi.org/10.1016/j.apgeochem.2011.05.005.
Jalali, L., Zarei, M., Gutiérrez, F., 2019. Salinization of reservoirs in regions with exposed evaporites. The unique case of Upper Gotvand Dam. Iran. Water Res. 157 https://doi.org/10.1016/j.watres.2019.04.015.
Jammes, S., Lavier, L., Manatschal, G., 2010. Extreme crustal thinning in the Bay of Biscay and the Western Pyrenees: From observations to modeling. Geochem. Geophys. Geosys., 11. https://doi.org/ 10.1029/2010GC003218.
Jochems, A.P., Pederson, J.L., 2015. Active salt deformation and rapid, transient incisión along the colorado river near moab. Utah. J. Geophys. Res. Earth Surf. 120, 730–744. https://doi.org/10.1002/2014JF003169.
Larrasoaña, J.C., Parés, J.M., Millán, H., Del Valle, J., Pueyo, E.L., 2003. Paleomagnetic, structural, and stratigraphic constraints on transverse fault kinematics during basin inversion: The Pamplona Fault (Pyrenees, north Spain). Tectonics, 22. https://doi.org/ 10.1029/2002TC001446.
Lauritzen, S.-E., Lauritsen, A., 1995. Differential diagnosis of paragenetic and vadose canyons. Cave Karst Sci. 21, 55–59.
Lenaroz, B., 1993. Geomorfología y Geología Ambiental de la Ribera de Navarra. University of Zaragoza. PhD Thesis.
Lescoutre, R., Manatschal, G., 2020. Role of rift-inheritance and segmentation for orogenic evolution: Example from the pyrenean-cantabrian system. BSGF-Earth Sci. B. 191, 18. https://doi.org/10.1051/bsgf/2020021.
Lescoutre, R., Manatschal, G., Muñoz, J., 2021. Nature, Origin, and evolution of the pyrenean-cantabrian junction. Tectonics 40. https://doi.org/10.1029/2020TC006134.
Luca, P., Matias, H., Carballo, J., Sineva, D., Pimentel, G., Tritlla, J., Cerdà, M., Loma, R., Jiménez, R., Pontet, M., Martinez, P., Vega, V., 2017. Breaking Barriers and Paradigms in Presalt Exploration: The Pão de Açúcar Discovery (Offshore Brazil). AAPG Memoir 113, 10. https://doi.org/1306/13572007M1133686.
Lucha, P., Cardona, P., Gutiérrez, F., Guerrero, J., 2008. Natural and human-induced dissolution and subsidence processes in the salt outcrop of the Cardona Diapir (NE Spain). Env. Geol. 53, 1023–1035. https://doi.org/10.1007/s00254-007-0729-3.
Lucha, P., Gutiérrez, F., Galve, J.P., Guerrero, J., 2012. Geomorphic and stratigraphic evidence of incision-induced halokinetic uplift and dissolution subsidence in transverse drainages crossing the evaporite-cored barbastro-balaguer anticline (EbroBasin, NE Spain. Geomorphology 171–172, 154–172. https://doi.org/10.1016/j.geomorph.2012.05.015.
Marín-Barba, P., Marquez, G., Gallego, J.L., Permanyer, A., 2014. Characterization of asphaltic oil occurrences from the southeastern margin of the basque-Cantabrian basin. Spain. Geol. Acta 12, 327–342. https://doi.org/10.1344/GeologicaActa2014.12.4.4.
Marrucci, M., Zeilinger, G., Ribolini, A., Schwanghart, W., 2018. Origin of knickpoints in an alpine context subject to different perturbing factors, stura valley, maritime alps (North-Western Italy). Geosciences 18, 443. https://doi.org/10.3390/geosciences8120443.
Miall, A.D., 1978. Lithofacies types and vertical profile models in braided river deposits: A summary, in: Miall, A.D. (Ed.), Fluvial Sedimentology. Canadian Society of Petroleum Geologists, Memoir 5, pp. 597-604.
Millán, H., 2004. Geometry and kinematics of compressional growth structures and diapirs in the La Popa basin of northeast Mexico: Insights from sequential restoration

of a regional cross section and three-dimensional analysis. Tectonics 23, TC5011. https://doi.org/10.1029/2003TC001540.
Miró, J., Muñoz, J.A., Manatschal, G., Roca, E., 2020. The Basque-cantabrian pyrenees: Report of data analysis. BSGF-Earth Sci. Bull. 191 https://doi.org/10.1051/bsgf/2020024.
Miró, J., Manatschal, G., Cadenas Martínez, P., Muñoz, J., 2021. Reactivation of a hyperextended rift system: The basque-cantabrian pyrenees case. Basin Res. 33 https://doi.org/10.1111/bre.12595.
Muñoz, J.A., 1992. Evolution of a continental collision belt: ECORS-Pyrenees crustal balanced cross-section, in: McKlay, K.R. (Ed.), Thrust tectonics. Chapman and Hall, New York, pp. 235-246.
Olive, A., López-Horgue, M.A., Baceta, J., Niñero, S., Villanueva, E., 2010a. Memoria y mapa geológico de Navarra de la hoja de Estella (140) a escala 1:25.000. Gobierno de Navarra, Departamento de obras públicas, transportes y comunicaciones, Pamplona.
Olive, A., Hernández, A., Baceta, J., Gómez, I., Niñerola, S., 2010b. Memoria y mapa geológico de Navarra de la hoja de Allo (172) a escala 1:25.000. Gobierno de Navarra, Departamento de obras públicas, transportes y comunicaciones, Pamplona.
Palmer, A.N., 2009. Cave Geology. Cave Books, Dayton.
Parenti, C., Baioni, D., García-Arnay, Á., Sevil, J., Luzzi, E., 2020. Closed depressions in Kotido crater, Arabia Terra, Mars. Possible evidence of evaporite dissolution-induced subsidence. Icarus 341, 113680. https://doi.org/10.1016/j.icarus.2020.113680.
Parés, J.M., Duval, M., Soria-Jáuregui, A., González-Amuchástegui, M.J., 2021. First chronological constraints for the high terraces of the upper ebro catchment. Quaternary 4, 25. https://doi.org/10.3390/quat4030025.
Parkhurst, D.L., Appelo, C.A.J., 2013, Description of input and examples for PHREEQC version 3: A computer program for speciation, batch-reaction, one-dimensional transport, and inverse geochemical calculations. U.S. Geological Survey Techniques and Methods, book 6, chap. A43, 497 p. https://pubs.usgs.gov/tm/06/a43/ (accessed 18 May 2023).
Pérez-Rivarés, F., Garcés, M., Arenas, C., Pardo, G., 2004. magnetostratigraphy of the miocene continental deposits of the montes de castejón (central Ebro Basin, Spain): Geochronological and paleoenvironmental implications. Geol. Acta 2, 221–234. https://doi.org/10.1344/105.000001429.
Perucha, M.A., Medialdea, A., Mediato, J.F., Salazar, A., 2015. Contribución al conocimiento de la cronología de los depósitos de terraza de los ríos Ebro e Híjar en la zona de Reinosa (Cantabria). In: Galve, J.P., Azañón, J.M., Pérez Peña, J.V., Ruano, P. (Eds.), Una Visión Global DEl Cuaternario, El Hombre Como Condicionante De Procesos Geológicos. Granada, XIV Reunión Nacional de Cuaternario, pp. 20–23.
Pflug, R., 1973. El diapiro de Estella. Minube 2–4, 171–202.
Pflug, R., Schöll, W.U., 1976. Un bloque de material jurásico metamorfizado en el Keuper del Diapiro de Estella (Navarra). Minube 4, 349–353.
Pinto, V., Casas, A., Rivero, L., Torne, M., 2005. 3D gravity modelling of the triassic salt diapirs of the cubeta alavesa (northern Spain). Tectonophysics 405, 65–75. https://doi.org/10.1016/j.tecto.2005.05.010.
Poprawski, Y., Basile, C., Agirrezabala, L., Jaillard, E., Gaudin, M., Jacquin, T., 2014. Sedimentary and structural record of the albian growth of the bakio salt diapir (the Basque Country, northern Spain). Basin Res. 12062 https://doi.org/10.1111/bre.12062.
Poprawski, Y., Christophe, B., Jaillard, E., Matthieu, G., Lopez, M., 2016. Halokinetic sequences in carbonate systems: An example from the middle albian bakio breccias formation (Basque Country, Spain). Sed. Geol. 334 https://doi.org/10.1016/j.sedgeo.2016.01.013.
R Development Core Team, 2020. R: A Language and Environment for Statistical Computing. R Foundation for Statistical Computing, Vienna.
Reimer, P.J., Austin, W.E.N., Bard, E., Bayliss, A., Blackwell, P.G., Ramsey, C.B., Butzin, M., Cheng, H., Edwards, R.L., Friedrich, M., Grootes, P.M., Guilderson, T.P., Hajdas, I., Heaton, T.J., Hogg, A.G., Hughen, K.A., Kromer, B., Manning, S.W., Muscheler, R., Palmer, J.G., Pearson, C., van der Plicht, J., Reimer, R.W., Richards, D.A., Scott, E.M., Southon, J.R., Turney, C.S.M., Wacker, L., Adolphi, F., Büntgen, U., Capano, M., Fahrni, S.M., Fogtmann-Schulz, A., Friedrich, R., Köhler, P., Kudsk, S., Miyake, F., Olsen, J., Reinig, F., Sakamoto, M., Sookdeo, A., Talamo, S., 2020. The IntCal20 northern hemisphere radiocarbon age calibration Curve (0–55 cal kBP). Radiocarbon 62, 725–757. https://doi.org/10.1017/RDC.2020.41.
Rigo, A., Vernant, P., Feigl, K.L., Goula, X., Khazaradze, G., Talaya, G., Morel, L., Nicolas, J., Baize, S., Chery, J., Sylvander, M., 2016. Present-day deformation of the Pyrenees revealed by GPS surveying and earthquake focal mechanisms until 2011. Geophys. J. Int. 201, 947–964. https://doi.org/10.1093/gji/ggv052.
Rouby, D., Raillard, S., Guillocheau, F., Bouroullec, R., Nalpas, T., 2002. Kinematics of a growth/raft system on the West African margin using 3-D restoration. J. Struc. Geol. 24, 783–796. https://doi.org/10.1016/S0191-8141(01)00108-0.
Rowan, M.G., Peel, F.J., Vendeville, B., Gaullier, V., 2012. Salt tectonics at passive margins: Geology versus models discussion. Mar. Pet. Geol. 37, 184–194. https://doi.org/10.1016/j.marpetgeo.2012.04.007.
Salvany, J.M., 1990. Introducción a las evaporitas triásicas de las cadenas periféricas de la cuenca del Ebro: Catalánides, Pirineo y Región Cantábrica. In: Orti, F., Salvany, J. M. (Eds.), Formaciones Evaporíticas De La Cuenca Del Ebro Y CaDenas Periféricas Y De La zona De Levante. Universidad de Barcelona, ENRESA-GPPG, pp. 9–20.
Sánchez-Morales, M., Pèlachs, A., Codron, J., Carracedo, V., Perez-Obiol, R., 2022. Landscape dynamics and fire regime since 17,550 cal yr BP in the Cantabrian region (La Molina peat bog, Puente Viesgo, Spain). Quat. Sci. Rev. 278, 107373. https://doi.org/10.1016/j.quascirev.2022.107373.
Santolaria, P., Vendeville, B.C., Graveleau, F., Soto, R., Casas-Sainz, A., 2015. Double evaporitic décollements: Influences of pinch-out overlapping in experimental thrust wedges. J. Struc. Geol. 76, 35–51. https://doi.org/10.1016/j.jsg.2015.04.002.
Serrano, A., Martínez del Olmo, W., 2004. Estructuras diapíricas de la zona meridional de la Cuenca Vasco-Cantábrica. In: Vera, J.A. (Ed.), Geología de España. Sociedad Geológica de España, Instituto Geológico y Minero de España, Madrid, pp. 334–338.
SITNA, 2023. Sistema de información territorial de Navarra. Gobierno de Navarra, https://idena.navarra.es/navegar/?lang=es (accessed 9 May 2023).
Stewart, S.A., 2006. Implications of passive salt diapir kinematics for reservoir segmentation by radial and concentric faults. Mar. Petr. Geol. 23, 843–853. https://doi.org/10.1016/j.marpetgeo.2006.04.001.
Taheri, K., Mohseni, H., Raeisi, E., Taheri, M., 2015. Sinkhole susceptibility mapping using the analytical hierarchy process (AHP) and magnitude–frequency relationships: A case study in hamadan province. Iran. Geomorphology 234. https://doi.org/10.1016/j.geomorph.2015.01.005.
Talbot, C.J., Aftabi, P., 2004. Geology and model of salt extrusion at Qun Kuh, central Iran. J. Geol. Soc. Lond. 161, 321–334. https://doi.org/10.1144/0016-764903-102.
Trudgill, B.D., 2011. Evolution of salt structures in the northern paradox basin: Controls on evaporite deposition, salt wall growth and supra-salt stratigraphic architecture. Basin Res. 23, 208–238. https://doi.org/10.1111/j.1365-2117.2010.00478.x.
Urabayen, P., Chasco, A., 2001. Estudio del karst yesífero en el diapiro de estella. Las formas exokársticas y su relación con la evolución vertical del mismo. Science Report. Ayuntamiento de Estella.
Uranga, S., Mañero, J., Dorronsoro, C., 1997. Comparación geoquímica y mineralógica del ripio de perforación del sondeo Izarra-1 (Estella, Navarra). Geogaceta 22, 207–210.
van Hinsbergen, D.J.J., van der Meer, D.G., Zachariasse, W.J., Meulenkamp, J.E., 2006. Deformation of western Greece during Neogene clockwise rotation and collision with Apulia. Int. J. Earth Sci. 95, 463–490. https://doi.org/10.1007/s00531-005-0047-5.
Vergés, J., Fernàndez, M., Martínez, A., 2002. The Pyrenean orogen: pre-, syn-, and post-collisional evolution. J. Virtual Exp., 8, 55-74. https://doi.org/ 10.3809/jvirtex.2002.00058.
Warren, J.K., 2016. Evaporites. A geological compendium, Springer, Berlin.
Warsitzka, M., Kley, J., Kukowski, N., 2015. Analogue experiments of salt flow and pillow growth due basement faulting and differential loading. Solid Earth 6, 9–31. https://doi.org/10.5194/se-6-9-2015.